PHYSICAL REVIEW FLUIDS **1**, 024201 (2016)

Lattice-Boltzmann simulation of inertial particle-laden flow around an obstacle

Hamed Haddadi
Department of Bioengineering, University of California at Los Angeles, 420 Westwood Plaza, Los Angeles, California 90095, USA

Shahab Shojaei-Zadeh
Mechanical and Aerospace Engineering, Rutgers, The State University of New Jersey, Piscataway, New Jersey 08854, USA

Jeffrey F. Morris*
Department of Chemical Engineering and Levich Institute for Physico-Chemical Hydrodynamics, City College of New York, New York, New York 10031, USA
(Received 24 February 2016; published 22 June 2016)

The lattice-Boltzmann method is used to compute the flow of a particle suspension of dilute volume fraction $\phi \leqslant 0.08$ around obstacles. The work focuses on the interaction of particles with the obstacle and the flow behavior in and around the recirculating wake behind the obstacle. Motivated by microfluidic experiments of dilute suspension flow over obstacles of circular, square, and other shapes showing depletion of particles in the wake behind the obstacle, we focus on the entry and exit from the wake for isolated particles, small groups of particles, and a suspension of many particles. All work is at conditions well below the Reynolds number for the transition to unsteady flow and vortex shedding. The dynamics of an isolated particle inside the recirculating wake flow exhibits motion toward a limit cycle near the outer boundary of the wake. By increasing particle density above the fluid and increasing the size of the particle, we determine the upper limits of these variables yielding a limit cycle trajectory. Hydrodynamic interaction between particles in a many-particle suspension is shown to lead to exchange of particles between the wake zone and free stream.

DOI: 10.1103/PhysRevFluids.1.024201

I. INTRODUCTION

The interaction of fluids with solid boundaries in inertial flow results in the formation of wakes and recirculating flow regions behind obstacles [1,2] or complex flow patterns around freely moving objects immersed in the flow [3–5]. For mixture flows containing dispersed particles, the available information is quite limited. One well-known effect is the generation of lift force on particles, which leads to lateral migration in the cross section of a conduit in pressure-driven flow [6,7]. However, despite decades of study of inertial lift force [8] by analytical [9,10], computational [11], and experimental methods [12], only limited mechanistic descriptions of inertial lift are available [13]. In the present work we discuss recently observed aspects of inertial flow of mixtures by studying the flow of a suspension of hard spheres over an obstacle. We are particularly interested in the interaction of particles with recirculating wakes behind obstacles, with the work here considering circular and square cylinders.

The formation of wakes and recirculating flow regions due to the inertial interaction of a fluid with solid boundaries is a classic phenomenon in Newtonian fluid dynamics. However, various questions arise for more complex fluids or mixtures and here we consider the simplest case of a

*morris@ccny.cuny.edu

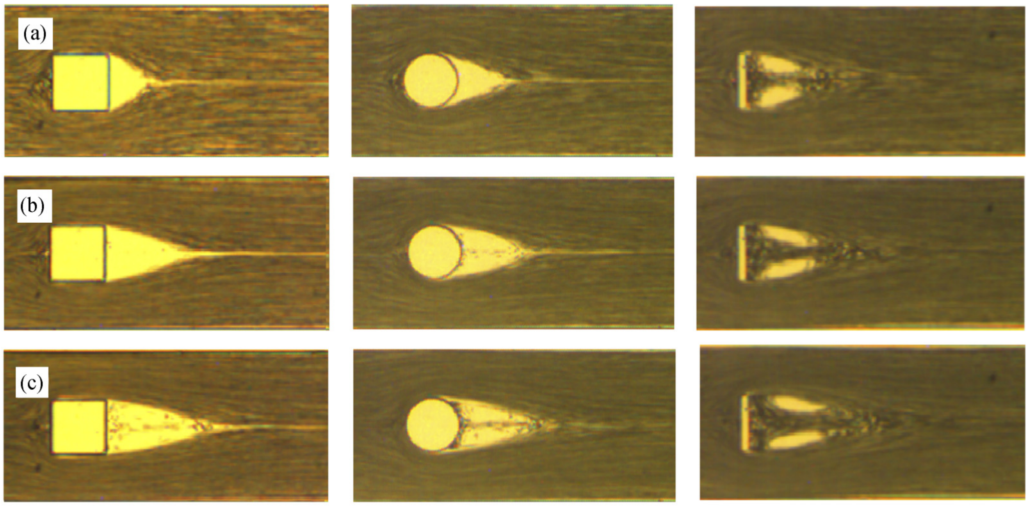

FIG. 1. Experimental observation of dilute (solid fraction $\phi \approx 0.08$) suspension flow over square, circular, and blade cylinders in a microchannel at (a) Re = 242, (b) Re = 363, and (c) Re = 484. Formation of a depleted wake is distinctly observed behind the square and circular objects, while the recirculation behind the blade entraps a large number of particles. In the microchannel, inertial effects are strongly suppressed, leading to larger Re to achieve extended wakes than expected for an axially extended cylinder.

suspension of rigid particles. For this case, the collision of particles with the obstacle, the onset of vortex shedding in the presence of particles, and the fluctuating force exerted on the obstacle by the mixture are aspects of the flow past the obstacle that are largely unknown. In the flow over the obstacle, the relative magnitude of inertial and viscous force is represented by the Reynolds number, defined as $\mathrm{Re} = \frac{uD}{\nu}$, where u is the average velocity, D is the obstacle diameter, and ν is the kinematic viscosity of the fluid. At sufficient Re, flow separation leads to a recirculating wake forming downstream of the obstacle and the behavior of suspended particles in and around the wake is of interest. Typical values of Re leading to recirculation are $\mathrm{Re} \geqslant 10$ for unbounded flow, while in flow in highly confined geometries, such as that found in microfluidic applications, the influence of inertia can be suppressed such that Re must be larger for recirculation to occur. The interaction of particles with recirculating zones is relevant in biofluid applications such as blood flow in arterial stenosis [14] and aneurysms [15] or growth of biofilm streamers [16]. Additionally, vortical flow in a confined microchannel has been utilized for separation of circulating tumor cells from blood samples [17].

Motivation for the present computational study comes from our experimental observation of dilute suspension flow over different geometry obstacles confined in a microchannel [18] (see Fig. 1). The length, width, and height of the microchannel are measured to be $X = 10$ mm, $Y = 465$ μm, and $Z = 60$ μm, respectively, and the obstacle is placed midway between inlet and outlet. In flow of a dilute suspension (solid fraction $\phi \approx 0.08$) of hard spheres confined in a microchannel, the interaction of particles with the recirculating flow region leads to a particle-depleted wake, with details of the depletion depending on obstacle shape. An almost empty wake region forms behind cylinders of circular and square generators spanning a straight microchannel. However, the wake behind a "blade" obstacle has particle-free portions, but still contains many particles. In the recent numerical simulation of suspension flow around a circular cylinder using a combined suspension balance-immersed boundary approach, the formation of the empty wake was also observed, in reasonable agreement with our previous experimental results [19]. One interesting aspect of suspension flow over an obstacle is particle exchange between the free stream and the recirculating flow region: Recall that there is no fluid mass exchanged across the material surface separating the wake and free stream in steady flow of a pure fluid over the obstacle. We focus our discussion on the basic case of dilute suspension flow over circular and square obstacles in an axially unbounded domain to interpret the formation of the depleted wake region and shed light on features of bulk flow over the obstacle. We will return in Sec. IV to briefly consider how confinement generates three-dimensional motion in the wake, which may amplify the particle exchange.

In our previous work on the behavior of suspension flow over an obstacle [18], we showed that a single neutrally buoyant particle released in the recirculating flow region moves to a limit cycle, at least partially rationalizing depletion of the core region of the wake. In the present work we consider a much broader range of particle sizes (relative to the obstacle) and particle densities to delineate conditions resulting in a limit cycle. We also provide the average distribution of particles around the obstacle and suspension velocity. It will be shown that the hydrodynamic interaction between particles in the wake and in the free stream is the basis for particle exchange between the recirculating flow region and the free stream.

We probe the flows using numerical simulation of suspension flow by the lattice-Boltzmann method (LBM), a versatile approach to studying flows of fluid-solid mixtures [20–25]. Applications of the LBM include the fluctuating hydrodynamics of polymers and colloids [26], noncolloidal and inertial suspensions of particles [27] (including ellipsoids [28]), flow of deformable particles [29], and mixture flows with interfacial tension effects [30]. The capability of resolving fluid flow combined with mesh refinement [31] is an advantageous feature of the LBM for the study of mixture flow in complex geometries. Despite these capabilities of the LBM, resolving flow of the suspension in the regime where collisions, whether between particles or between particles and boundaries, are a factor remains a challenge. In this work we present a method for resolving the collision and partial rebound of particles after breakdown of hydrodynamic lubrication. The model is employed for particle-particle and particle-obstacle collisions.

We begin with a brief description of the lattice-Boltzmann method and computational parameters, followed by implementation of the collision model for circular and square cylinders. With recent advancement of computational methods for simulating suspension flow over the circular cylinder, implementing a physical collision model for the interaction of particles with obstacles is crucial. We validate our method for flow over an obstacle using two benchmark examples for which experimental results are available: wake size versus Reynolds number for a circular cylinder [1,2] and the restitution coefficient for collision of a sedimenting particle with a plane wall [32]. We then present our findings on the dynamics of a single particle released inside the recirculating wake, with emphasis on limit cycle trajectories. Deviations of particle trajectories from the limit cycle, which are caused by the hydrodynamic interaction between multiple particles, are demonstrated. Aspects of the bulk flow such as the average distribution of particles around the obstacle, average velocities, and velocity fluctuations will be presented, followed by a discussion and concluding remarks.

A. Governing equation and computational parameters

The nondimensional forms of the fluid phase governing equations are

$$\nabla \cdot \boldsymbol{u} = 0, \tag{1}$$

$$\mathrm{Re}\left(\frac{\partial \boldsymbol{u}}{\partial t} + \boldsymbol{u} \cdot \nabla \boldsymbol{u}\right) = -\nabla p + \nabla^2 \boldsymbol{u}, \tag{2}$$

where the length has been made dimensionless by the diameter of the obstacle D, velocity by the average axial velocity of the fluid at inlet $\bar{U}$, and pressure by $\eta \bar{U}/D$. Newtonian dynamics govern the motion of particles. The translational $\boldsymbol{U}_i$ and rotational $\boldsymbol{\Omega}_i$ velocities of particles are calculated from

$$\boldsymbol{F}_i = m_i \frac{d\boldsymbol{U}_i}{dt}, \tag{3}$$

$$\boldsymbol{T}_i = I_i \frac{d\boldsymbol{\Omega}_i}{dt}, \tag{4}$$

where $\boldsymbol{F}_i$ and $\boldsymbol{T}_i$ are the force and torque on particle i, which has mass m_i and a moment of inertia I_i.

Numerical simulations have been conducted in a rectangular computational domain with mean flow in the X direction and the obstacle cross section on the XY plane. The obstacle extends along the Z direction. The unconfined computational box is periodic in all directions with sizes $L \times H \times W$ along the X, Y, and Z directions, respectively. The size of the obstacle facing the flow is $D = 64$ lattice units (l.u.), whether the diameter of the circular cylinder or the side length of the square. The particle sizes are $d = 5.85$, 10.1, and 12.9 l.u. per diameter, yielding the size ratio $\delta = d/D = 0.1$, 0.15, and 0.2 for these three different sizes of particles.

B. Simulation method

We have employed the LBM for simulating suspension flow. The method for simulating moving particles immersed in a fluid was first presented by Ladd [20,21] and has undergone significant further development [22,23]. The LBM for hard-sphere suspensions simulates the fluid motion using the discrete Boltzmann equation, while as noted Newtonian dynamics are applied to the particles. The hydrodynamic traction at the particle surface couples fluid and solid phases. The fluid phase is composed of fictitious particles, termed lattice-Boltzmann (LB) particles, which move along the various directions of a lattice. The state of the fluid is described by a continuous distribution function $n_i(\boldsymbol{r},t)$, which represents the mass density of the fluid at each lattice node $\boldsymbol{r}$ along a certain lattice direction i, at time t. The velocity of the LB particles along lattice direction i is denoted by $\boldsymbol{c}_i$. The isotropy of the fluid phase requires a three-dimensional multispeed lattice. In the present work, the D3Q19 lattice model has been used, which specifies a three-dimensional lattice with 19 velocities, including one for the case of zero velocity. The mass density of the fluid phase ρ, the momentum density $\boldsymbol{j} = \rho\boldsymbol{u}$, and momentum flux $\boldsymbol{\Pi} = \rho\boldsymbol{u}\boldsymbol{u}$ are defined as moments of the distribution function

$$\rho = \sum_i n_i, \quad \boldsymbol{j} = \sum_i n_i \boldsymbol{c}_i, \quad \boldsymbol{\Pi} = \sum_i n_i \boldsymbol{c}_i \boldsymbol{c}_i. \tag{5}$$

The evolution of the distribution function $n_i(\boldsymbol{r},t)$ is governed by the lattice-Boltzmann equation

$$n_i(\boldsymbol{r} + \boldsymbol{c}_i \Delta t, t + \Delta t) = n_i(\boldsymbol{r},t) + \sum_j \boldsymbol{\Omega}_{ij}\left(n_i - n_i^{\mathrm{eq}}\right), \tag{6}$$

where $\boldsymbol{\Omega}_{ij}$ denotes the linearized collision operator representing the change in the distribution function due to molecular collisions at each time step Δt. With the Maxwell-Boltzmann distribution function as the equilibrium form, the Navier-Stokes equations are recovered for low-Mach-number flows. In flow over the obstacle, the Mach number can be defined as the ratio of the average axial velocity at the inlet to the speed of sound as $\mathrm{Ma} = \frac{\bar{U}}{c_s}$. The solid-liquid boundary condition has been implemented by the link-bounceback method. The particle surface cuts the links between lattice nodes and boundary nodes are placed halfway along the links. The distribution function on the nodes adjacent to the boundary nodes is modified according to

$$n_{-i}(\boldsymbol{r}, t + \Delta t) = n_i^*(\boldsymbol{r},t) - \frac{2a^{c_i}\rho_0 \boldsymbol{u}_b \cdot \boldsymbol{c}_i}{c_s^2}, \tag{7}$$

where $-i$ indicates the velocity in the opposite direction, $\boldsymbol{c}_i = -\boldsymbol{c}_i$. The a^{c_i} are coefficients of the velocity in different lattice directions and n_i^* is the postcollision distribution function. The velocity of the solid boundary is denoted by $\boldsymbol{u}_b$ and the speed of sound c_s in the lattice is $\sqrt{1/3}$. The momentum exchange between solid and fluid leads to a force on the particle, given by

$$\boldsymbol{f}_b\left(\boldsymbol{r}_b, t + \frac{1}{2}\Delta t\right) = \frac{\Delta x^3}{\Delta t}\left[2n_i^* - \frac{2a^{c_i}\rho_0 \boldsymbol{u}_b \cdot \boldsymbol{c}_i}{c_s^2}\right]\boldsymbol{c}_i, \tag{8}$$

where Δx is the lattice spacing. The velocity of the solid boundary

$$\boldsymbol{u}_b = \boldsymbol{U} + \boldsymbol{\Omega} \times (\boldsymbol{r}_b - \boldsymbol{R}) \tag{9}$$

is calculated using the center-of-mass velocity $\boldsymbol{U}$, angular velocity $\boldsymbol{\Omega}$, location of the center of mass $\boldsymbol{R}$, and coordinates of the boundary nodes $\boldsymbol{r}_b = \boldsymbol{r} + \frac{1}{2}\boldsymbol{c}_i \Delta t$. By summing over forces and torques on all boundary nodes, the total force and torque on the particle are calculated as

$$\boldsymbol{F} = \sum_{\boldsymbol{r}_b} \boldsymbol{f}(\boldsymbol{r}_b), \quad \boldsymbol{T} = \sum_{\boldsymbol{r}_b} (\boldsymbol{r}_b - \boldsymbol{R}) \times \boldsymbol{f}(\boldsymbol{r}_b), \tag{10}$$

which are then used to update particle translational and rotational velocities using mass and moment of inertia. Particle trajectories are obtained by integrating translational velocity.

Considering that the particle surface nodes are placed halfway along the links, the link-bounceback method generates a discrete representation of the spherical particle. With increase of the resolution, i.e., the number of lattice units per particle diameter, a more accurate representation of the particle surface is obtained. Due to discrete representation of the particle surface, there is a difference between the hydrodynamic diameter of the particle and the physical diameter on the lattice. The sphere samples various boundary links as it moves on the lattice, generating a slight variation in the particle representation. The difference between hydrodynamic and physical diameters is denoted by Δ_h and can be obtained by simulating fluid flow over a fixed sphere and computing the hydrodynamic drag. The value of Δ_h also depends on the viscosity of the fluid [22]. For $\delta = 0.1$, 0.15, and 0.2 particles and for the fluid kinematic viscosity $\nu = 0.01$ used in our simulations, $\Delta_h = 0.224$, 0.243, and 0.25 l.u., respectively.

At very small surface separations, where there is no intervening fluid node, pairwise short-range hydrodynamic forces between particles are computed in the form [22]

$$\boldsymbol{F}_{\text{lub}} = -\frac{6\pi\eta(a_1 a_2)^2}{(a_1 + a_2)^2} \hat{\boldsymbol{r}}\hat{\boldsymbol{r}} \cdot \boldsymbol{V} \left(\frac{1}{h} - \frac{1}{h_N} \right), \tag{11}$$

taking $a_1 = a_2 = a$ as the particle radius and η as the fluid viscosity, where $\boldsymbol{V} = \boldsymbol{U}_2 - \boldsymbol{U}_1$ is the pair relative velocity and $\boldsymbol{r} = \boldsymbol{r}_2 - \boldsymbol{r}_1$ is the center-of-mass separation between particles 1 and 2 located at $\boldsymbol{r}_1$ and $\boldsymbol{r}_2$ with $\hat{\boldsymbol{r}} = \frac{\boldsymbol{r}}{|\boldsymbol{r}|}$. The surface separation between particles is defined as $h = |\boldsymbol{r}| - 2a$. For surface separations larger than lubrication cutoff h_N, which is defined as $0.015d$, force is computed as the sum of forces on the boundary nodes. For surfaces closer than the overlap criterion, defined here at $7.5 \times 10^{-7}d$, the collision forces govern the motion of particles.

For a square cylinder the lubrication force between each face of the square and a spherical particle is implemented using the resistance matrix for particle-wall lubrication. We will simply assume that hydrodynamic lubrication does not act on a particle approaching a sharp corner, so only collision forces govern the interaction of the particle and corner.

C. Numerical simulation: Suspension flow around an obstacle

Before presenting the results of the simulation of suspension flow over rigid circular and square obstacles, we demonstrate the accuracy of the numerical method using benchmark results. These are unbounded flow of a pure fluid over a circular cylinder and the particle elastic collision with a wall [32], described using a restitution coefficient. The accuracy of the LBM solver is examined by computing the size of the wake behind a circular cylinder at various Re and comparing with the experimental results of Taneda [1,2] for pure fluid flow over a cylinder. Results presented in Fig. 2(a) show excellent agreement for wake size between our computations and experimental measurements. In Fig. 3 we show the streamlines around the circular and square obstacles projected on a background shaded according to the velocity magnitude for Re = 11 and 17, for which all simulations of particle-laden flow have been conducted.

To study inertial particle-laden flow over an obstacle, in addition to a lubrication model for close surface separations, we also implement a numerical collision model. A rigorous solution for the breakdown of hydrodynamic lubrication for the inertial collision of a neutrally buoyant particle with a surface is not yet available. However, we assume that hydrodynamic lubrication breaks down and collision forces govern the motion of particles at very small surface separations. An elastic

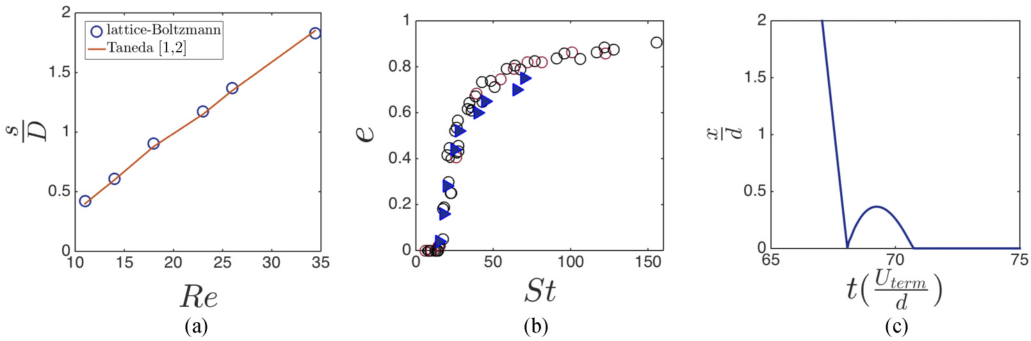

FIG. 2. Validations. (a) Comparison of the numerical measurement of the wake size behind a circular cylinder s, scaled by the cylinder diameter D, with the experimental results of Taneda [1,2]. (b) Comparison of the coefficient of restitution generated using the proposed collision model (triangles) for a $\delta = 0.15$ particle with experimental data (circles) from Li *et al.* [32]. (c) Simulated trajectory of a sedimenting particle of $\delta = 0.15$ toward a plane wall at St $= 50$. After collision, the particle bounces back from the wall with a velocity in the opposite direction and decelerates sufficiently that a second bounce is not seen. Dimensionless time $t(\frac{U_{\text{term}}}{d})$ is measured from the release of the particle from rest.

collision model represents a more realistic physics for motion of inertial particles at close surface separations, compared with applying a repulsive singular or spring force on particles, which has been conventionally used to compute motion at very small surface separations. In the singular forcing method, a repulsive force of the form C/r^{α} is applied on the particles at small surface separations. Similarly, the spring force is represented by $C\boldsymbol{r}$. In addition to the arbitrariness introduced by the parameters C and α, the singular or spring forcing can lead to rebound of colliding particles with significantly large speeds, which may even exceed the speed of particles before collision. The method we employ to calculate the motion of particles at close surface separations is based on calculating hydrodynamic lubrication, followed by the collision force for very small gaps between surfaces. Therefore, the lubrication forces act on particles for $h < h_N$ and for smaller separations the elastic collision force prevents the overlap between surfaces. The numerical implementation of the lubrication force that acts between two close solid surfaces is shown above as (11) [22] and its accuracy has been examined in previous works [4,27]. Despite its crucial role in collisional flows

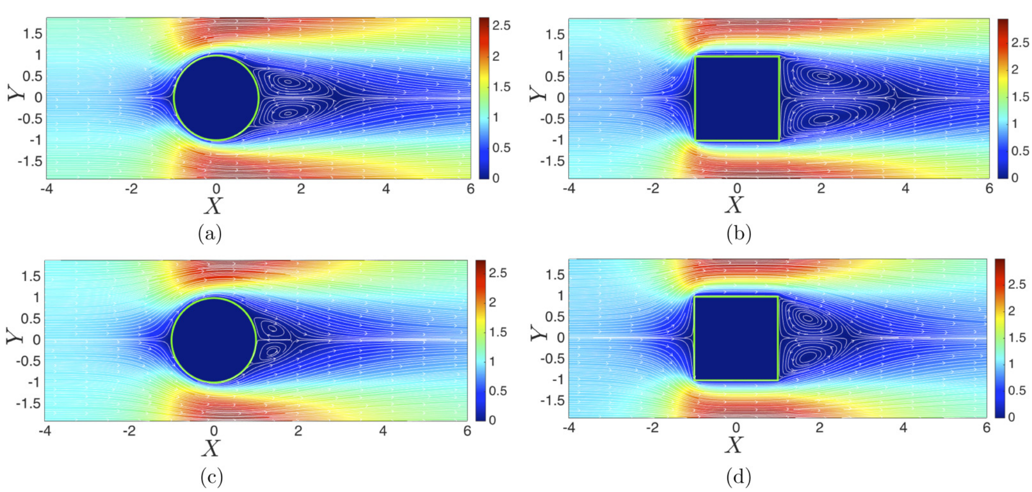

FIG. 3. Streamlines around circular and square cylinders overlaid on the velocity magnitude for (a-b) Re $= 17$ and (c-d) Re $= 11$.

such as particle-laden flow in fractures, mud flow, fluidized bed reactors. and microchannel flow, the collision of neutrally buoyant particles and rigid walls has not been extensively studied. For comparison to our modeling, we use the restitution coefficients determined experimentally for dense particles settling and rebounding from a wall in otherwise quiescent fluid [32].

For particle-laden flow, the collision has been modeled by *hard-sphere* and *soft-sphere* approaches. As opposed to a soft-sphere collision, where mechanical properties of colliding surfaces are taken into account in calculating the model parameters, the mechanical properties are not considered in a hard-sphere collision model [33]. Here we use the hard-sphere approach as a baseline for elastic collision between surfaces. The inertia of the particle relative to viscous forces is represented by the Stokes number, defined as $\mathrm{St} = \frac{1}{9}(\frac{\rho_p}{\rho_f})\mathrm{Re}_{\mathrm{sed}}$ for sedimentation, where $\frac{\rho_p}{\rho_f}$ is the density ratio of the solid to liquid phase [32]. Using the terminal velocity of the particle before impact U_{term} and particle diameter d, the Reynolds number is defined as $\mathrm{Re}_{\mathrm{sed}} = \frac{U_{\mathrm{term}} d}{\nu}$.

For a perfectly elastic collision in the absence of energy dissipation, the kinetic energy of particles is completely restored after impact, i.e., the velocity upon normal impact is simply reversed. When mediated by a fluid, even for elastic solids, the impact of particles does not result in full recovery of the initial energy and the recoil speed is below the approach speed. This behavior is captured using a coefficient of restitution e, which for the collision between particles 1 and 2 is defined as $\frac{U_2^{t+} - U_1^{t+}}{U_1^{t-} - U_2^{t-}}$, where $t-$ and $t+$ specify the times just before and after impact, respectively. For the collision of particles with a stationary solid surface, the restitution coefficient of the particle is defined similarly as $e = \frac{U_p^{t+}}{U_p^{t-}}$. A comparison of the results of our numerical model for collision with the experimental data of Li *et al.* [32] is presented in Fig. 2(b). While there is a slight difference for $\mathrm{St} > 50$, the collision model recovers the experimental results accurately for $\mathrm{St} < 50$, where the work that follows will be focused. The trajectory of a sedimenting particle released from rest in a quiescent fluid is exhibited in Fig. 2(c). The particle accelerates from rest and reaches the terminal velocity U_{term} before impact. After impact, the particle bounces back with a velocity in the opposite direction and decelerates before settling back to rest without a bounce.

The numerical model for elastic collisions is now considered, beginning with two hard spherical particles of potentially different sizes for generality. The motion of particles after collision is governed by *impulse* linear and angular momentum equations. In the absence of friction between solid surfaces, the effect of collision on angular momentum can be ignored. After reduction of the distance between two surfaces to less than $7.5 \times 10^{-7} d$, the hard-sphere collision algorithm governs the motion of particles at close surface separations. For two particles with center-of-mass position vectors $\boldsymbol{r}_1$ and $\boldsymbol{r}_2$ and center-of-mass separation vector $\boldsymbol{r} = \boldsymbol{r}_1 - \boldsymbol{r}_2$, the relative velocity of particles can be projected on the line of centers to find the velocities in the collision frame of reference $u_r = (\boldsymbol{U}_1 - \boldsymbol{U}_2) \cdot \hat{\boldsymbol{r}}$, where $\hat{\boldsymbol{r}} = \frac{\boldsymbol{r}}{|\boldsymbol{r}|}$ is the unit vector along line of centers of the particles. Using the reduced mass $\mu = \frac{m_1 m_2}{m_1 + m_2}$, where m_1 and m_2 specify the mass of particles 1 and 2, respectively, the momentum before collision can be calculated as $p_i = \mu u_r \hat{r}_i$, where i indicates the X, Y, or Z direction. The velocity components of particles 1 and 2 after collision are calculated as $U_i^{1,t+} = -p_i/m_1$ and $U_i^{2,t+} = p_i/m_2$.

The collision between spherical particles and a circular cylinder [see Fig. 4(a)] is handled similarly, except that in the calculation of the relative distance between objects only X and Y components of the position vector are considered (the circular cylinder dimension in the Z direction is infinite). The collision of spherical particles and each face of a square cylinder is implemented as a sphere-wall collision. Each face of the square is characterized by the normal vector to the surface $\boldsymbol{n}_i$, where $i = \pm x$ and $\pm y$ for faces parallel to the Y and X axes, respectively. The separation vector between a particle and $\boldsymbol{n}_x$ face is $\boldsymbol{r}_w = (x_{\mathrm{c.m.}} - r_x^w)\boldsymbol{n}_x$, where $x_{\mathrm{c.m.}}$ is the X component of the particle center of mass and r_x^w is the location of the wall surface in the X direction. Here we denote the separation vector between a particle and a plane wall by $\boldsymbol{r}_w$. The normal component of the relative velocity of the particle and wall is obtained by projecting the particle velocity $\boldsymbol{U}$ along the separation unit vector $u_r = \boldsymbol{U} \cdot \frac{\boldsymbol{r}_w}{|\boldsymbol{r}_w|}$. Using the momentum before impact $p_x = m u_r r_x$, the velocity of the particle

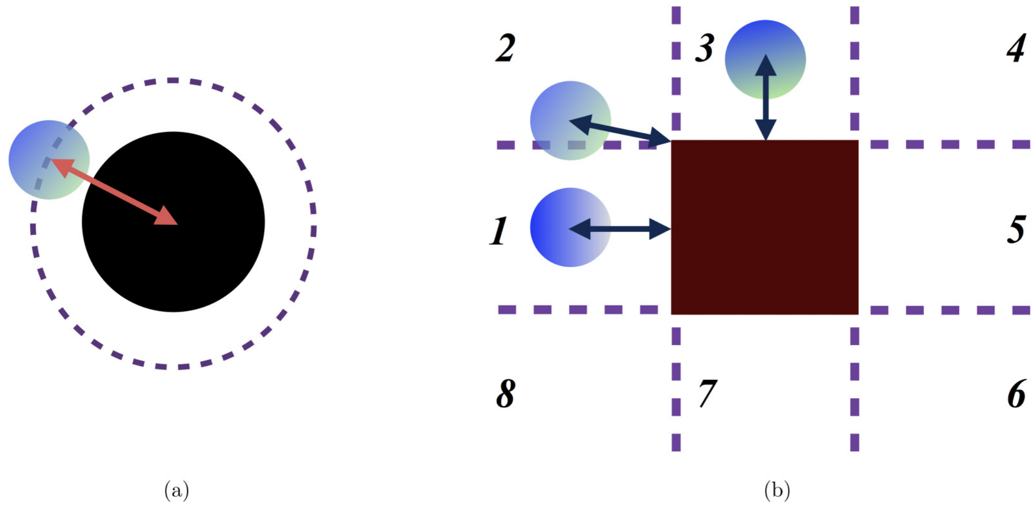

FIG. 4. (a) Hard-sphere collision with a circular cylinder. (b) Collision of the spherical particle with a square cylinder.

after the impact can be obtained as $U_x^{t+} = \frac{p_x}{m}$, where m is the particle mass. A collision between a particle and a wall with the normal in the Y direction is implemented in the same way.

The collision scheme for a particle colliding with the corner of a square obstacle is sketched in Fig. 4(b). Depending on the center-of-mass location, a particle can collide with X or Y walls or the corner. Therefore, the space around the square obstacle is divided into eight regions, as illustrated in Fig. 4(b). Here we explain the obstacle collision model for a particle located in regions 1, 2, or 3, specified as $|\Delta y| = |y_{\text{c.m.}} - r_y^x| \leqslant D/2$, $D/2 \leqslant |\Delta y| \leqslant D/2 + r$, and $\Delta x = |x_{\text{c.m.}} - r_y^x| \leqslant D/2$. Considering symmetry, an identical collision scheme is implemented for other zones (4–8). When the particle center of mass is located in zone 1 or 3, the particle collides with X or Y walls respectively, with a collision model explained before. For a particle approaching the square obstacle from zone 2, the collision frame of reference is constructed along the vector connecting the particle center of mass and the corner of the square obstacle. Velocities of the particle before and after the impact are calculated using the particle-wall collision model.

II. SINGLE-PARTICLE DYNAMICS INSIDE THE WAKE

In our previous work [18] we showed that a neutrally buoyant particle released inside a steady wake of a circular cylinder moves toward a limiting stable closed orbit near the wake boundary with the free stream; this is a true limit cycle as it has a basin of attraction both inside and outside the closed orbit. For particles released inside the orbit, deviation of particles (at least for ρ_p and ρ_f matched as shown in that work) from closed orbits leads to outward motion toward the limit cycle, at a rate that depends on the inertia of the particle. The inertia is characterized by a Stokes number $\text{St} = \frac{\rho_p}{\rho_f}\text{Re}_p$, where Re_p is defined using the diameter of the particle $\text{Re}_p = \frac{\bar{U}d}{\nu}$, where we recall that $\bar{U}$ is the average velocity at the inlet of the computation box. (Note the difference from the definition of the Stokes number for the sedimentation problem mentioned previously.) The formation of the limit cycle for neutrally buoyant particles was observed for $\delta = 0.1$, 0.15, and 0.2 [18].

In the present work we expand consideration to particles of different density for $\delta = 0.1$ and 0.15. This allows examination of an approximate range of particle properties leading to limit cycle formation. With an increase of either the density or size, both leading to larger St, the particle can be made to exit the wake zone rather than approaching a stable limit cycle. Particle trajectories are investigated for the wake behind both circular and square cylinders.

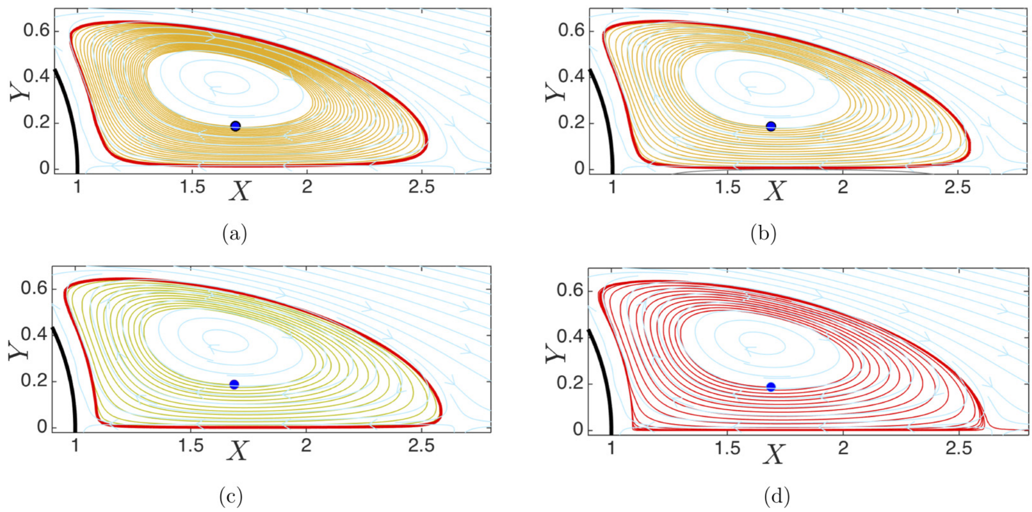

FIG. 5. Limit cycles at varying particle densities. The trajectory of a $\delta = 0.1$ particle released inside the steady-state wake behind a circular cylinder at Re = 17 forms a limit cycle at (a) $\frac{\rho_p}{\rho_f} = 1$, (b) $\frac{\rho_p}{\rho_f} = 2.2$, and (c) $\frac{\rho_p}{\rho_f} = 3.4$, but does not at (d) $\frac{\rho_p}{\rho_f} = 3.6$. The initial location of the particle is marked on the trajectory and the solid line specifies the limit cycle trajectory.

Figure 5 shows the trajectories for particles of $\delta = 0.1$ and different densities released at the same location well inside the recirculating wake behind a circular cylinder at Re = 17. The starting point is close to the wake core and particle motions begin after formation of a steady recirculating flow. It is perhaps surprising that for $\delta = 0.1$, a particle with a large density of $\frac{\rho_p}{\rho_f} = 3.4$ moves on a stable limit cycle trajectory. With a further increase of the particle density to $\frac{\rho_p}{\rho_f} = 3.6$ the limit cycle is no longer observed and the outward displacement continues until the particle exits the wake region. It is also shown that with increasing density, the limit cycle trajectory forms closer to the wake boundary and, as expected, the larger the density of the particle, the more rapid the outward motion. Increasing either the particle density or size leads to larger outward displacement in each orbit and for a sufficiently large value of either variable, the particle will exit the wake region. As shown in Fig. 6 for trajectories of a $\delta = 0.15$ particle at various densities, with increasing particle diameter, the exit from the wake zone occurs at a lower density ratio of $\frac{\rho_p}{\rho_f} = 2.4$, compared to $\frac{\rho_p}{\rho_f} = 3.6$ for $\delta = 0.1$ particles. Here we point out that in our work, the Stokes numbers of particle exit for $\delta = 0.1$ and 0.15 particles are 10.56 and 12.85, respectively. The mentioned values are obtained by using $\frac{\rho_p}{\rho_f} = 3.4$ and 2.4 for the density ratio. Considering that we have incremented the density ratio by 0.2 to identify conditions for wake exit, the Stokes numbers do not correspond to the exact value leading to particle exit. Presenting a critical value of St for particle exit requires single-particle trajectory samplings for various particle sizes and densities for a wide range of Re and this is outside the scope of this work. For the wake behind a square cylinder at Re = 17, Fig. 7 shows trajectories of neutrally buoyant particles of $\delta = 0.1$ and 0.15. While the outward motion of the $\delta = 0.1$ particle reaches a stable limit cycle, the larger particle exits the wake region.

A basin of attraction must exist both interior and exterior to a limit cycle. Figures 5 and 6 have already shown that trajectories starting inside the limit cycle spiral outward. In Fig. 8, trajectories released outside the limit cycle are shown to also move inward to approach the limit cycle trajectory. Here we demonstrate sample exterior trajectories at the highest density ratio for which we computed a limit cycle trajectory for $\delta = 0.1$ ($\rho_p/\rho_f = 3.4$) and 0.15 ($\rho_p/\rho_f = 2.2$) to corroborate formation of a limit cycle. While we have not explored in detail the form of the attractive basin outside the limiting trajectory, as this becomes sensitive to our imperfect release mechanism, presumably this basin is reduced to zero volume for a critical density ratio, e.g., $3.4 < \rho_{p,\mathrm{crit}}(\delta = 0.1)/\rho_f < 3.6$ as

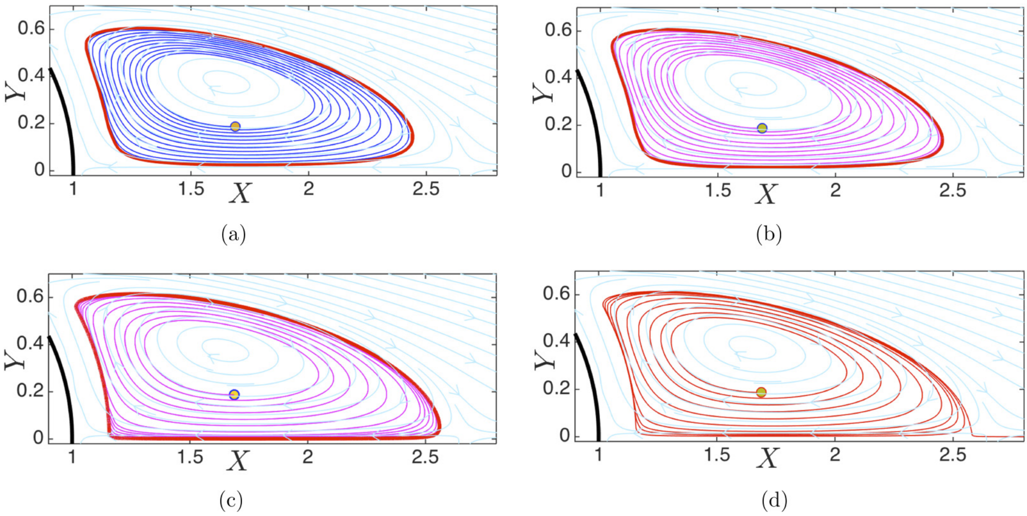

FIG. 6. Limit cycles at varying particle density. Shown is the trajectory of a single particle of size ratio relative to the obstacle $\delta = 0.15$, released inside the steady-state wake behind a circular cylinder at Re $= 17$ for (a) $\frac{\rho_p}{\rho_f} = 1$, (b) $\frac{\rho_p}{\rho_f} = 1.2$, (c) $\frac{\rho_p}{\rho_f} = 2.2$, and (d) $\frac{\rho_p}{\rho_f} = 2.4$. The initial location of the particle is marked on the trajectory and the solid line specifies the limit cycle trajectory.

illustrated in Fig. 5; we note that this critical value of the density is expected to be dependent upon the particle size.

In Fig. 9 the migration rate of a single particle toward the limit cycle is compared for different obstacle geometries, particle sizes, and particle densities. All of these rates of migration are determined for Re $= 17$, so the time scale of the bulk flow is the same in every case, i.e., $t^* = \frac{t\bar{U}}{D}$. The migration rate of a $\delta = 0.1$ particle towards the limit cycle is faster in the wake behind a square obstacle, as shown in Fig. 9(a). We present the effect of particle size for neutrally buoyant particles of $\delta = 0.1, 0.15$, and 0.2 in Fig. 9(b). Larger particles approach the limit cycle faster. In Fig. 9(c) we compare the rate of migration for $\delta = 0.15$ particles of $\frac{\rho_p}{\rho_f} = 1, 1.6$, and 2.2, where a faster motion toward the limit cycle trajectory is observed for higher-density particles.

III. DILUTE SUSPENSION FLOW OVER AN OBSTACLE

A. Formation of depleted wake region

We addressed the mechanism leading to the formation of a particle-depleted region behind a circular cylinder in our previous work [18]. The outward displacement in each orbit results in margination of particles close to wake boundaries, as shown in Fig. 10 for particles released from

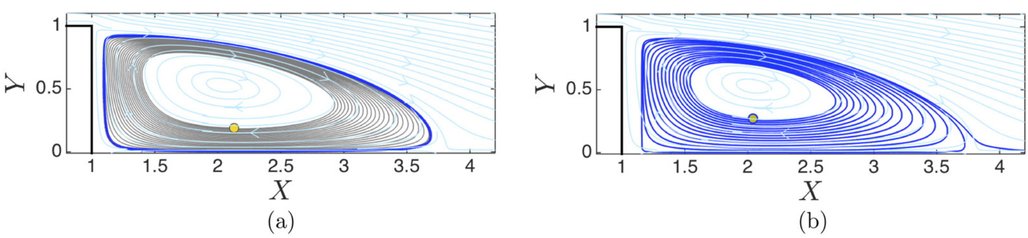

FIG. 7. Trajectory of a single neutrally buoyant particle released inside the steady-state wake behind a square cylinder at Re $= 17$ for (a) $\delta = 0.1$, which reaches a limit cycle, and (b) $\delta = 0.15$, which exits from the wake.

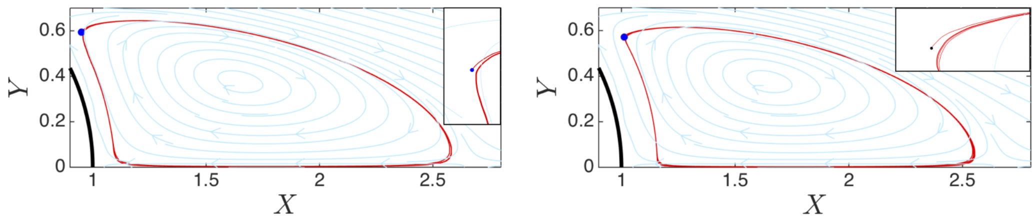

FIG. 8. Trajectory of a single particle with higher density than the fluid released in the exterior region of the limit cycle trajectory behind a circular cylinder at Re = 17 for (a) $\delta = 0.1$ and $\rho_p/\rho_f = 3.4$ and (b) $\delta = 0.15$ and $\rho_p/\rho_f = 2.2$. Exterior trajectories move inward toward the limit cycle. Magnified pictures show the release points more clearly.

random initial locations inside the wake [Figs. 10(a) and 10(b)]. The interaction of particles with one another results in deviation from the limit cycle trajectory [Figs. 10(b) and 10(c)]. Considering that the boundary between the recirculating zone and the free stream changes due to the presence of particles and is not a clearly defined surface, the wake boundary (i.e., the separatrix between the recirculating zone and free stream) for pure fluid is used in our calculations to define whether particles are inside the wake.

In our previous work, depletion of the wake was shown for $\phi = 0.04$, 0.06, and 0.08 suspensions flowing over a circular cylinder at Re = 17. Recent numerical simulation of the flow of a $\phi = 0.1$ suspension over a circular cylinder exhibits the formation of a depleted region behind the obstacle [19]. In the present work, the formation of the depleted region is studied for both circular and square cylinders and the particle exchange between the free stream and the recirculating flow region is examined more critically. Although the experimental study of dilute suspension flow over the obstacle has been conducted in a confined microchannel, here we investigate the more basic case of unbounded suspension flow over long (periodically replicated) square and circular cylinders. Confinement leads to the formation of a swirling fluid motion inside the wake and across its boundary, which can influence the particle exchange; this will be considered below.

Depletion of the wake zone in the flow of a $\phi = 0.08$ suspension over an obstacle is shown in Fig. 11. Simulation snapshots show the distribution of particles in the wake region. The number of particles in the wake N at each sampling time is normalized by the number of particles initially located in the wake N_i. The initial reduction of the number of particles is due to startup of the suspension flow and a slower reduction in the number of particles continues after the flow is fully developed. The rate of depletion is more pronounced for the square obstacle.

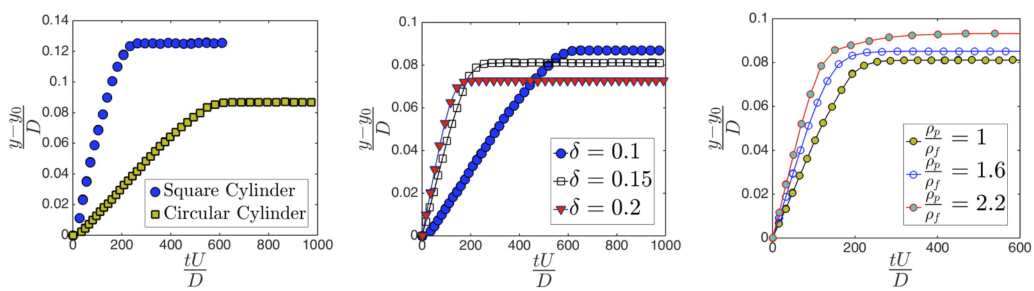

FIG. 9. Comparison of the migration rate toward limit cycle for (a) $\delta = 0.1$ particles in the wake behind a square and circular obstacle at Re = 17, (b) $\delta = 0.1$, 0.15, and 0.2 neutrally buoyant particles released inside the wake behind a circular cylinder at Re = 17, and (c) $\delta = 0.15$ with different density ratios in the wake behind a circular cylinder at Re = 17.

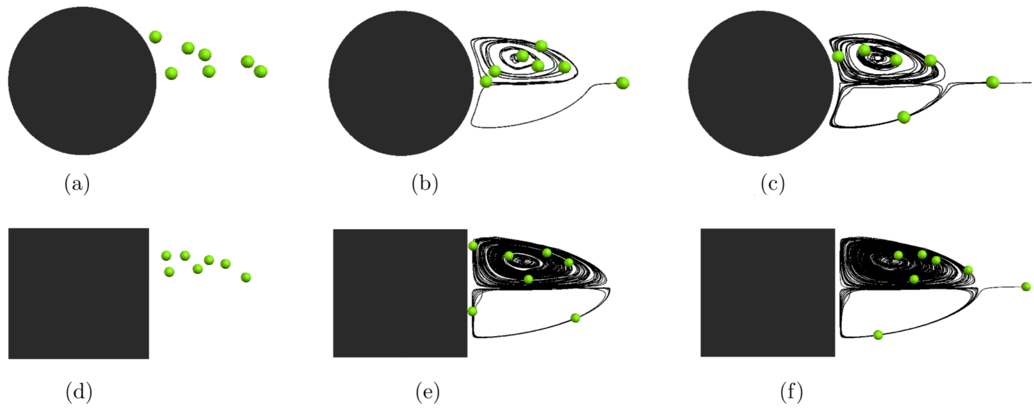

FIG. 10. Three snapshots of particle motion inside the wake behind (a)–(c) a circular and (d)–(f) a square cylinder at Re = 17: (a) and (d) the initial configuration, (b) and (e) outward motion of particles that constantly interact with each other. (c) and (f) Particle interactions result in deviation from the limit cycle trajectory. Continuation of simulation to longer times leads to more particles exiting.

While there is no mass exchanged between the free stream and recirculating flow in the steady flow of a pure fluid over an obstacle, the presence of particles causes microscale unsteadiness in the flow and this leads to exchange of fluid and particles. The mass exchange mechanism between the wake and free stream is due to the formation of transient lobes on the separatrix. The lobe dynamics mechanism has been discussed in great detail for flow over open cavities [34,35], where unsteadiness generated by periodic fluid flow or disturbance of particles has been shown to lead to amplification of the "lobe-turnstile" mechanism. Variation of the wake boundaries due to suspension flow is not conveniently determined by the current resolution of our numerical method. However, we can demonstrate the mass exchange between the free stream and wake region by sampling particle trajectories that move between the recirculation and the free stream. With the entrapment in or exit of particles from the wake, fluid mass is also exchanged. We present sample trajectories for a $\phi = 0.08$ suspension over the obstacles in Fig. 12. While a single neutrally buoyant particle in the free stream does not enter the recirculating zone [18] and a particle released in the wake forms a limit cycle

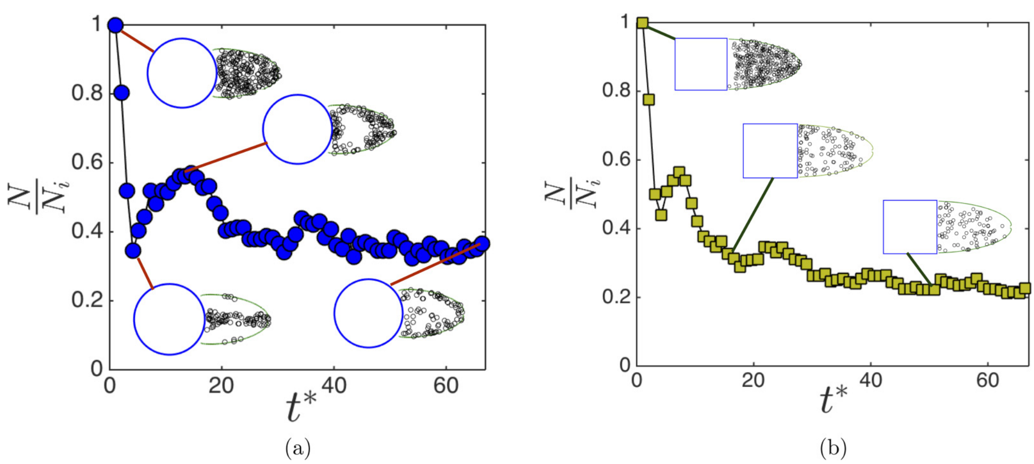

FIG. 11. Number of particles in the wake region versus dimensionless time $t^* = \frac{t\bar{U}}{D}$ for flow of a $\phi = 0.08$ suspension over (a) a circular cylinder and (b) a square cylinder.

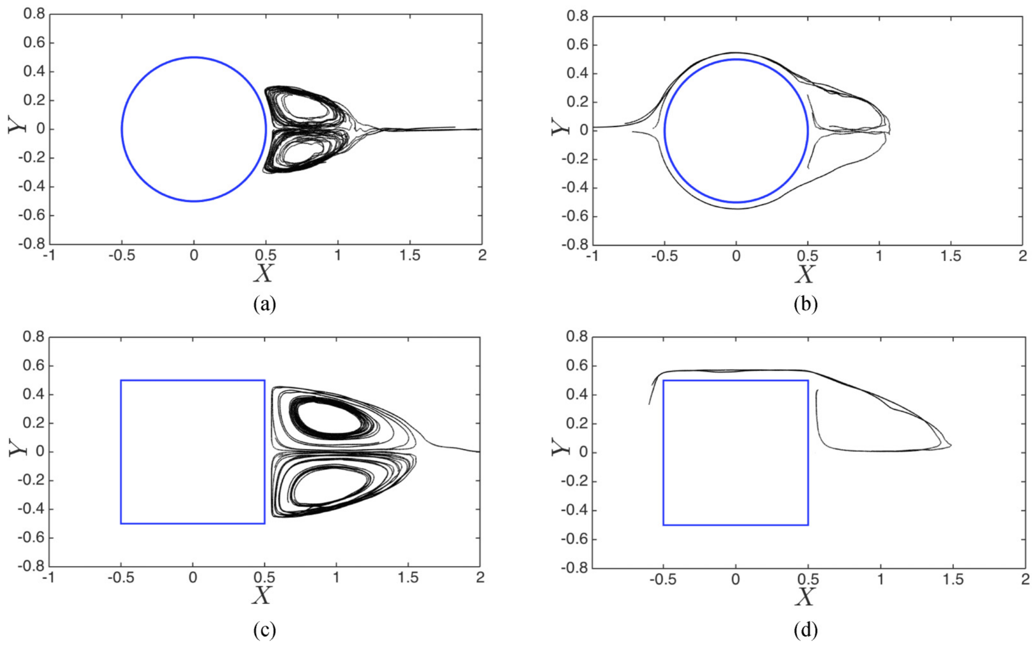

FIG. 12. Sampled particle trajectories showing a particle exchange between the free stream and the recirculating flow region at Re = 17 and $\phi = 0.08$. (a) and (c) Particles orbit inside the wake and exit the recirculating zone. (b) and (d) Particle entry to the wake.

close to the wake boundaries, particles can enter, orbit inside the wake, or exit the recirculating flow region in the flow of the dilute suspension.

B. Average motion of particles around the obstacle

In addition to the formation of a depleted wake region behind the obstacle, the bulk motion of the suspension is affected by features of the flow over an obstacle, such as the presence of a stagnation point at the front of the obstacle. Flow features are manifested in the distribution of particles around the obstacle and the average suspension velocity. Other aspects of bulk flow over an obstacle have been discussed for suspension flow over a cylinder [19]. We discuss characteristics of the bulk motion of a $\phi = 0.08$ suspension in flow over circular and square obstacles for Re = 11 and 17. Similar features have also been observed in the flow of a $\phi = 0.04$ suspension. Figure 13 displays the average distribution of particles around circular and square obstacles. The averages are calculated at Re = 11 and 17, for size ratio of $\delta = 0.1$, by sampling the center-of-mass coordinates of particles and dispensing the coordinates into a histogram over a long time span, i.e., 200 flow time scales. Considering that flow is invariant in the Z direction, the histogram is populated by X and Y coordinates of all particles. The sampling begins after reaching steady state in the bulk flow. A similar sampling procedure is used to generate the spatial distributions of suspension average velocity.

The formation of a depleted wake region behind the obstacle can be clearly observed from the average distributions. The size of the depleted region depends on Re and obstacle geometry. It has been shown that the size of the recirculating flow region is larger for a square obstacle (Fig. 3). Similarly, a larger depleted region forms behind the square obstacle in the presence of particles. Although the obstacle is symmetrically placed in the domain, a slight statistical asymmetry is observed in the distribution of particles inside the wake region. This may arise from fluctuations in the initial distribution or from fluctuations in the exchange of particles between the wake and

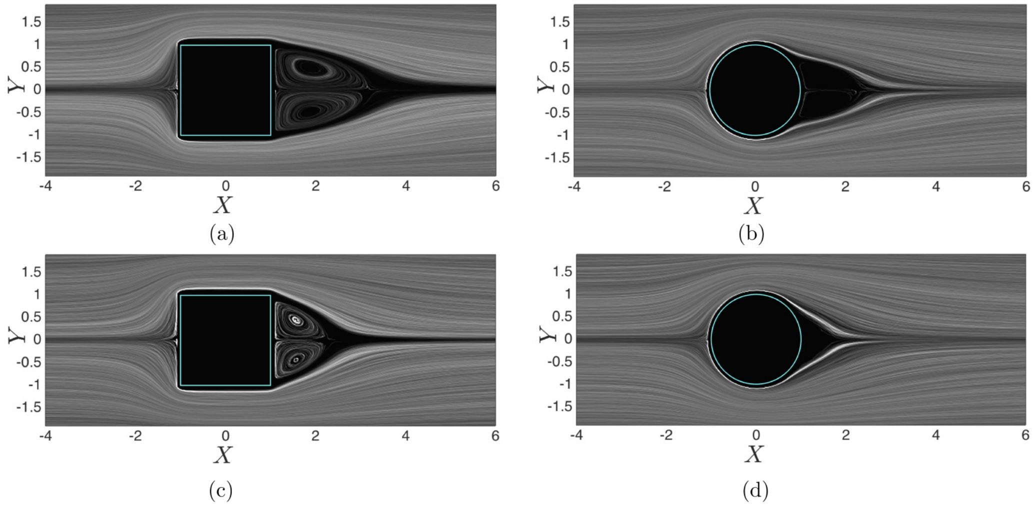

FIG. 13. The average distribution of $\delta = 0.1$ particles around square and circular cylinders at (a) and (b) Re $= 17$ and (c) and (d) Re $= 11$.

recirculating flow region. If many initial conditions were averaged over time, asymmetry would be expected to tend to zero.

Particles approaching the stagnation point at the obstacle front are divided symmetrically (on average) and pass the obstacle. Divided streams of particles join in the downstream to form a weld line, which has a more pronounced presence in distributions around the square obstacle. Because of the periodic boundary conditions in all directions, the downstream weld line affects the upstream distribution of particles, especially in flow over the square. We study features of suspension flow around an obstacle by presenting the average velocity of particles. To demonstrate the average velocity of particles, we exhibit the average particle pathlines overlain on the magnitude of the average particle velocity in Fig. 14. Similar to pure fluid flow over an obstacle, where the magnitude

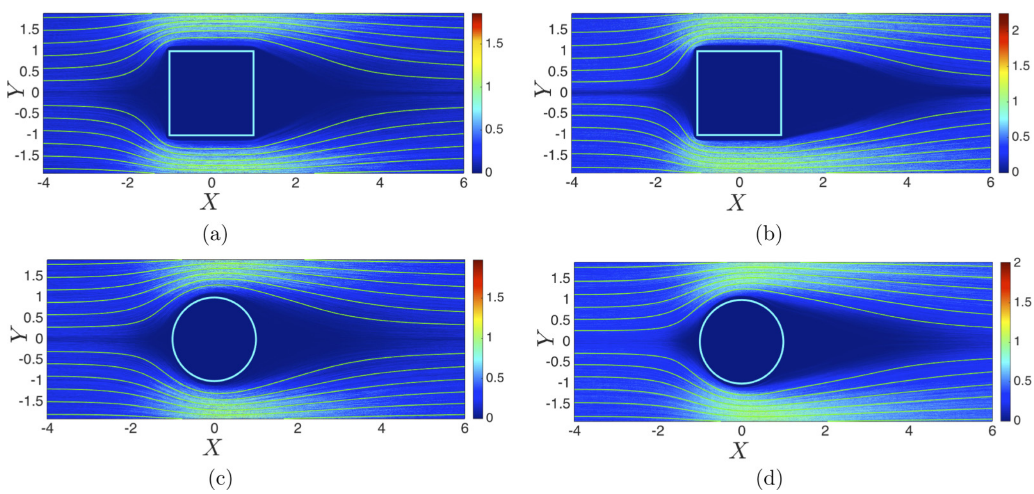

FIG. 14. Average suspension velocity in flow over (a) and (b) square and (c) and (d) circular cylinders at (a) and (c) Re $= 11$ and (b) and (d) Re $= 17$. The velocity is normalized by the inlet average in generating the color scale.

of the velocity is higher at regions of large streamline deflection, deviation of particle trajectories during interaction with the obstacle leads to an increase of particle velocity. Close to the stagnation point, the average bulk velocity is small. The magnitude of the average velocity is small in the recirculating flow region, as Fig. 9 indicates by a significantly longer time scale than the free stream flow for orbital motion of a particle inside the wake.

IV. CONCLUSION

In this work we have examined various aspects of dilute suspension flow over an obstacle. Although flow over an obstacle has long been studied, flow of a dilute suspension over the obstacle raises many questions, with the formation of a depleted region in the wake behind the obstacle the motivating issue in this work. We have also demonstrated that suspension flow leads to particle exchange between the recirculating flow region and the free stream. Starting from the dynamics of an isolated particle, we demonstrated that an isolated finite-size particle released inside the wake migrates outward until reaching a limit cycle trajectory. With increasing density and size, particles eventually exit the wake without forming a stable limit cycle trajectory. By releasing multiple neutrally buoyant particles inside the wake region, we showed that outward motion and hydrodynamic interaction between particles cause deviation from the stable limit cycle orbit and thus may lead to particle exit from the wake region. Additionally, fluctuations generated by hydrodynamic interactions between particles in the free stream may lead to entrapment of particles inside the recirculating flow zone. The overall effect of the outward motion and exchange of particles between the free stream and the wake is a reduction of the number of particles in the wake and formation of a depleted zone. We have studied dilute suspension flow over circular and square cylinders by implementation of a numerical model for particle-particle and particle-obstacle collisions.

Although experimental observations of the depleted wake region have been made in a confined microchannel geometry, we have presented our explanations for the more general case of dilute suspension flow over an obstacle in unbounded geometries. Here we briefly explain the effect of confinement on suspension flow over the obstacle. Of course, in depth examination of confined suspension flow over the obstacle requires an extended discussion and is beyond the scope of the present work.

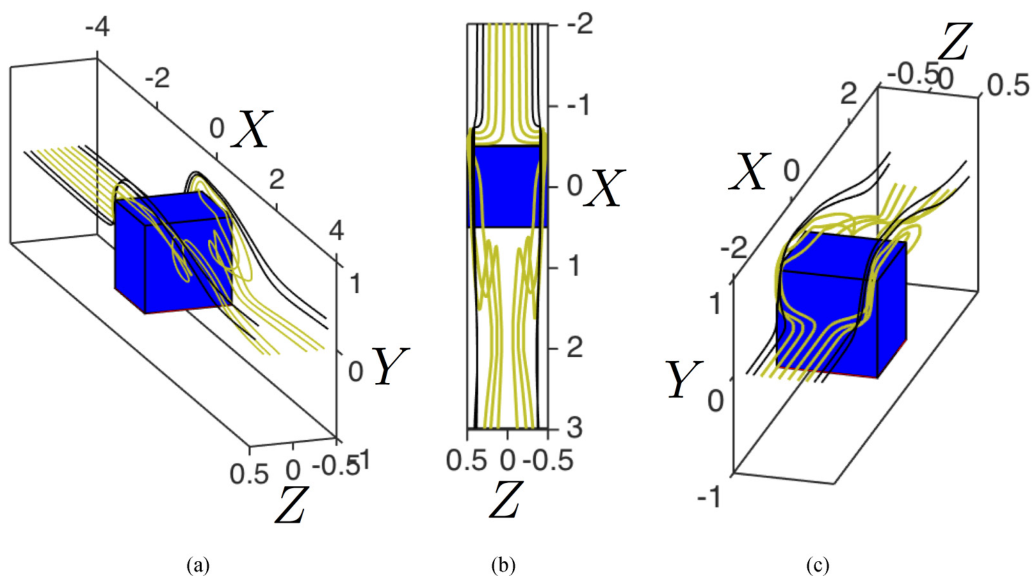

(a) (b) (c)

FIG. 15. Confinement-induced spiraling flow into the wake region, which can lead to particle entry into the wake, viewed from three angles.

The primary effect of confinement in flow of a *pure fluid* over an obstacle in a confined geometry is the formation of spiraling currents into the recirculating flow region. While there is no fluid exchange between the wake and free stream in the flow of a pure fluid over an obstacle in unbounded geometries, fluid streamlines spiral into the wake region in a wall-bounded conduit. We present spiraling currents in pure fluid flow over a square cylinder in Fig. 15. In order to exhibit details of streamlines in a confined channel, we show the spiraling currents from three different angles. It is observed that fluid streamlines enter the wake behind the obstacle from corners of the obstacle and spiral toward the center of the channel. The spiraling fluid flow can influence the motion of particles and lead to significant entry into the wake region, particularly for a blade obstacle. Studying the particle or fluid exchange in confined flow can be a direction for future studies on the subject.

ACKNOWLEDGMENTS

The work of H.H. was funded by NSF Grant No. CBET 0847271. J.F.M. was supported by NSF Grant No. CBET 0847271 and by NSF PREM (Grants No. DMR 0934206 and No. DMR 1449568). This research was also supported by a grant of computer time from the City University of New York High Performance Computing Center under NSF Grants No. CNS-0855217, No. CNS-0958379, and No. ACI-1126113.

[1] S. Taneda, Experimental observation of the wake behind a sphere at low Reynolds numbers, J. Phys. Soc. Jpn. **11**, 1104 (1956).

[2] S. Taneda, Experimental observation of the wake behind cylinders and plates at low Reynolds numbers, J. Phys. Soc. Jpn. **11**, 302 (1956).

[3] G. Subramanian and D. Koch, Inertial effects on the transfer of heat or mass from neutrally buoyant spheres in a steady linear velocity fields, Phys. Fluids **18**, 073302 (2006).

[4] H. Haddadi and J. F. Morris, Topology of pair-sphere trajectories in finite inertia suspension shear flow and its effects on microstructure and rheology, Phys. Fluids **27**, 043302 (2015).

[5] R. K. Singh and K. Sarkar, Inertial effects on the dynamics, streamline topology and interfacial stresses due to a drop in shear, J. Fluid Mech. **683**, 149 (2011).

[6] G. Segré and A. Silberberg, Behaviour of macroscopic rigid spheres in Poiseuille flow. Part 1. Determination of local concentration by statistical analysis of particle passages through crossed light beams, J. Fluid Mech. **14**, 115 (1962).

[7] G. Segré and A. Silberberg, Behaviour of macroscopic rigid spheres in Poiseuille flow. Part 2. Experimental results and interpretation, J. Fluid Mech. **14**, 136 (1962).

[8] P. G. Saffman, The lift on a small sphere in a slow shear flow, J. Fluid Mech. **22**, 385 (1965).

[9] E. S. Asmolov, The inertial lift on a spherical particle in a plane Poiseuille flow at large channel Reynolds number, J. Fluid Mech. **381**, 63 (1999).

[10] J. P. Matas, J. F. Morris, and E. Guazzelli, Lateral force on a rigid sphere in large-inertia laminar pipe flow, J. Fluid Mech. **621**, 59 (2009).

[11] D. Di Carlo, J. F. Edd, K. J. Humphry, H. A. Stone, and M. Toner, Particle Segregation and Dynamics in Confined Flows, Phys. Rev. Lett. **102**, 094503 (2009).

[12] J. P. Matas, J. F. Morris, and E. Guazzelli, Inertial migration of rigid spherical particles in Poiseuille flow, J. Fluid Mech. **515**, 171 (2004).

[13] K. Hood, S. Lee, and M. Roper, Inertial migration of a rigid sphere in three-dimensional Poiseuille flow, J. Fluid Mech. **765**, 452 (2015).

[14] J. Berry, A. Santamarina, J. E. Moore, Jr., S. Roychowdhury, and W. Routh, Experimental and computational flow evaluation of coronary stents, Ann. Biomed. Eng. **28**, 386 (2000).

[15] V. Rayz, L. Boussel, M. Lawston, G. Acevedo-Bolton, L. Ge, W. Young, R. Higashida, and D. Saloner, Numerical modeling of the flow in intracranial aneurysms: Prediction of regions prone to thrombus formation, Ann. Biomed. Eng. **36**, 1793 (2008).

[16] S. Yazdi and A. Ardekani, Bacterial aggregation and biofilm formation in a vortical flow, Biomicrofluidics **6**, 044114 (2012).
[17] S. C Hurr, A. J. Mach, and D. Di Carlo, High-throughput size-based rare cell enrichment using microscale vortices, Biomicrofluidics **5**, 022206 (2011).
[18] H. Haddadi, S. Shojaei-Zadeh, K. Connington, and J. F. Morris, Suspension flow past a cylinder: Particle interactions with recirculating wakes, J. Fluid Mech. **760**, R2 (2014).
[19] T. Dbouk, A suspension balance direct-forcing immersed boundary model for wet granular flows over obstacles, J. Nonnewton Fluid Mech. **230**, 68 (2016).
[20] A. J. C. Ladd, Numerical simulations of particulate suspensions via a discretized Boltzmann equation. Part 1. Theoretical foundation, J. Fluid Mech. **271**, 285 (1994).
[21] A. J. C. Ladd, Numerical simulations of particulate suspensions via a discretized Boltzmann equation. Part 2. Numerical results, J. Fluid Mech. **271**, 311 (1994).
[22] N. Q. Nguyen and A. J. C. Ladd, Lubrication corrections for lattice-Boltzmann simulations of particle suspensions, Phys. Rev. E **66**, 046708 (2002).
[23] C. K. Aidun, Y. Lu, and E. Ding, Direct analysis of particulate suspensions with inertia using the discrete Boltzmann equation, J. Fluid Mech. **373**, 287 (1998).
[24] T. Rosen, F. Lundell, and C. K. Aidun, Effect of fluid inertia on the dynamics and scaling of neutrally buoyant particles in shear flow, J. Fluid Mech. **738**, 563 (2014).
[25] C. K. Aidun and J. R. Clausen, Lattice-Boltzmann method for complex flows, Annu. Rev. Fluid Mech. **42**, 439 (2010).
[26] O. Berk Usta, A. J. C Ladd, and J. E. Butler, Lattice-Boltzmann simulations of the dynamics of polymer solutions in periodic and confined geometries, J. Chem. Phys. **122**, 094902 (2005).
[27] H. Haddadi and J. F. Morris, Microstructure and rheology of finite inertia neutrally buoyant suspensions, J. Fluid Mech. **749**, 431 (2014).
[28] E. Ding and C. K. Aidun, The dynamics and scaling law for particles suspended in shear flow with inertia, J. Fluid Mech. **423**, 317 (2000).
[29] R. M. MacMeccan, J. R. Clausen, G. P. Neitzel, and C. K. Aidun, Simulating deformable particle suspensions using a coupled lattice-Boltzmann and finite-element method, J. Fluid Mech. **618**, 13 (2009).
[30] K. W. Connington, M. Z. Miskin, T. Lee, H. M. Jaeger, and J. F. Morris, Lattice Boltzmann simulations of particle-laden liquid bridges: Effects of volume fraction and wettability, Int. J. Multiphase Flow **76**, 32 (2015).
[31] A. Fakhari and T. Lee, Finite-difference lattice Boltzmann method with a block-structured adaptive-mesh-refinement technique, Phys. Rev. E **89**, 033310 (2014).
[32] X. Li, M. L. Hunt, and T. Colonius, A contact model for normal immersed collisions between a particle and a wall, J. Fluid Mech. **691**, 123 (2012).
[33] N. G. Deen, M. Van Sint Annaland, M. A. Van Der Hoef, and J. A. M. Kuipers, Review of discrete particle modeling of fluidized beds, Chem. Eng. Sci. **62**, 28 (2007).
[34] M. Horner, G. Metcalfe, S. Wiggins, and J. M. Ottino, Transport enhancement mechanisms in open cavities, J. Fluid Mech. **452**, 199 (2002).
[35] S. C. Jana, G. Metcalfe, and J. M. Ottino, Experimental and computational studies of mixing in complex Stokes flows: The vortex mixing flow and multicellular cavity flows, J. Fluid Mech. **269**, 199 (1994).